Double-island Coulomb blockade in (Ga,Mn)As nanoconstrictions

S. Geißler,[1] S. Pfaller,[2,*] M. Utz,[1] D. Bougeard,[1] A. Donarini,[2] M. Grifoni,[2] and D. Weiss[1]
[1]*Institute for Experimental Physics, University of Regensburg, 93040 Regensburg, Germany*
[2]*Institute for Theoretical Physics, University of Regensburg, 93040 Regensburg, Germany*
(Received 24 February 2015; revised manuscript received 27 April 2015; published 22 May 2015)

We report on a systematic study of the Coulomb-blockade effects in nanofabricated narrow constrictions in thin (Ga,Mn)As films. Different low-temperature transport regimes have been observed for decreasing constriction sizes: the Ohmic, the single-electron tunneling (SET), and a completely insulating regime. In the SET, complex stability diagrams with nested Coulomb diamonds and anomalous conductance suppression in the vicinity of charge degeneracy points have been observed. We rationalize these observations in the SET with a double ferromagnetic island model coupled to ferromagnetic leads. Its transport characteristics are analyzed in terms of a modified orthodox theory of Coulomb blockade which takes into account the energy dependence of the density of states in the metallic islands.

DOI: 10.1103/PhysRevB.91.195432 PACS number(s): 72.25.−b, 73.23.Hk, 73.63.Kv

I. INTRODUCTION

(Ga,Mn)As, discovered by Ohno *et al.* [1] nearly two decades ago, is by now the best studied ferromagnetic semiconductor [2–4]. An interesting aspect of this material are large magnetoresistance effects which were discovered in nanofabricated narrow constrictions in thin (Ga,Mn)As films [5–10]. While the effects were initially interpreted in terms of the tunneling magnetoresistance (TMR) [5] and tunneling anisotropic magnetoresistance (TAMR) [6], it was proven later that the interplay with Coulomb blockade is also relevant in narrow (Ga,Mn)As constrictions [10,11]. The origin of this Coulomb-blockade anisotropic magnetoresistance (CBAMR) effect is substantial nanoscale fluctuations in the hole density [2] forming puddles of high hole density separated by low conducting regions. (Ga,Mn)As is known to be a strongly disordered material. Its hole density is close to the metal-insulator transition. Little variations in the hole density caused by local potential fluctuations can lead to an intrinsic structure consisting of metallic islands separated by insulating areas. It was shown that the magnetoresistance depends, in the presence of Coulomb blockade, not only on an applied gate voltage but can also be tuned by changing the direction of the applied magnetic field [10,11]. The latter results from the dependence of the Fermi energy on changes in the magnetization $\delta\vec{M}$ and was modeled phenomenologically by Wunderlich *et al.* [10]. If transport occurs through a narrow nanoconstriction, single-electron tunneling (SET) between islands of high carrier density becomes relevant. Thus, it is not surprising that the bias and temperature dependence of the magnetoresistance for different magnetization directions could be fitted with a model for granular metals in which metallic islands are separated by insulating regions [11]. Because of the nanoscale size of the involved "metallic" islands, the Coulomb-charging energy U is the dominating energy for transport across the nanoconstriction at low temperatures and small-bias voltages V_b. Since usually more than one island is involved in transport, Coulomb-blockade diamonds, where the resistance is plotted as a function of both bias and gate voltage, revealed a very complex and irregular pattern. Up to now, a detailed experimental and theoretical analysis of the Coulomb-blockade effects in (Ga,Mn)As nanoconstrictions in the single-electron-transistor regime is still missing.

The aim of this work is a systematic study of the Coulomb-blockade effects in nanofabricated narrow constrictions in thin (Ga,Mn)As films. By means of a two-step electron beam lithography (EBL) technique, we fabricated well-defined nanoconstrictions (NC) of different sizes. Depending on channel width and length, for a specific material, different low-temperature transport regimes could be observed, namely, the Ohmic regime, the single-electron tunneling regime, and a completely insulating regime. In the SET regime, complex stability diagrams with nested Coulomb diamonds and anomalous conductance suppression in the vicinity of charge degeneracy points have been observed. In order to understand these observations we propose, for a specific nanoconstriction, a model consisting of two ferromagnetic islands coupled to ferromagnetic leads. We study its transport characteristics within a modified orthodox theory of Coulomb blockade which takes into account the energy dependence of the density of states in the metallic islands.

The paper is structured as follows: Section II explains the fabrication process of the samples. In Sec. III, the measurement setup is presented. The next section, Sec. IV, summarizes the results of the measurements, giving a first interpretation in terms of a double-island structure within a classical orthodox model of Coulomb blockade [12–17]. In Sec. V, we present the details of the ferromagnetic double-island model, study its transport characteristics, and make a direct comparison with the experimental results in Sec. VI A. Conclusions are drawn in Sec. VII.

II. SAMPLE FABRICATION

Our NC devices were fabricated in a top-down approach starting from a (Ga,Mn)As layer with a Mn content of approximately 5%. The (Ga,Mn)As layer we used had a thickness of 15 nm and was grown by low-temperature molecular beam epitaxy on top of a (001)-GaAs substrate. In contrast to the experiments of Schlapps *et al.* [11], we used as-grown (Ga,Mn)As samples without additional annealing before the

*sebastian1.pfaller@ur.de

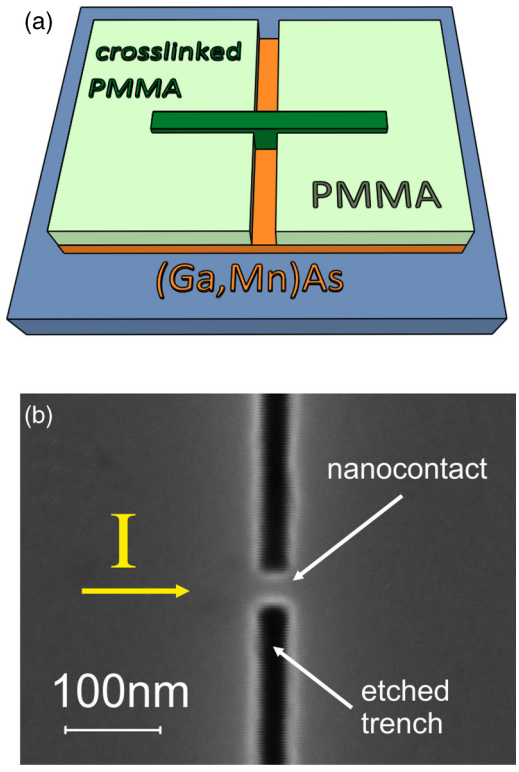

FIG. 1. (Color online) (a) Schematic of the PMMA mask (green/light green) defined by a two-step EBL process for etching the NC structure into a (Ga,Mn)As layer (orange) on top of a semi-insulating GaAs substrate (blue). (b) Electron micrograph of an NC device after ion-beam-etching and resist removal.

sample preparation. First of all, we defined contact pads for the source and drain contacts as well as alignment marks for the nanopatterning. This was done using optical lithography followed by thermal evaporation of 10 nm Ti and 90 nm Au in a standard liftoff technique. After that, the NC was defined by means of EBL and subsequent chemically assisted ion-beam etching using Cl_2. A two-step EBL process, which allows a precise control of the geometry of the nanocontact and a reliable processing, was developed and is described in Appendix A.

The structure of the poly-methyl-methacrylate (PMMA) mask, used for the two-step process, is sketched in Fig. 1(a). It mainly consists of the crosslinked PMMA line (dark green) of the first, high dose (3×10^4 C/cm) exposure step as well as of a narrow gap line from the second, usual exposure step, which separates the (Ga,Mn)As layer into two parts used as source and drain contacts. The two parts are connected with each other only at the NC, where the lines of the two exposure steps cross each other. This procedure allows us to define the width as well as the length of the NC by two single lines within independent exposure steps. This completely rules out the inter-proximity-effect between different exposed elements and reduces the minimum size of the NC to the smallest achievable linewidth of the two EBL steps. Compared to a single-step process, our approach is robust with respect to minor electron dose variations and thus well reproducible. Because of this, we were able to fabricate a large number of comparable devices and even to control the geometry of the NC with a precision of a few nanometers. Figure 1(b) shows an electron micrograph of the central part of a typical NC device taken after the chemically assisted ion-beam etching and resist removal using a low-energy oxygen plasma. After the nanopatterning we covered the whole sample with a 30-nm-thick Al_2O_3 layer grown by a low-temperature atomic layer deposition process at a temperature of 90 °C. The Al_2O_3 layer acts on the one hand as the gate dielectric and on the other hand it protects the tiny NC against oxidation. The top-gate contact was defined by optical lithography and covers not only the NC, but also the center part of the whole device. It consists, similarly to the source and drain contacts, of a 10/90-nm-thick Ti/Au stack evaporated thermally and structured using a standard liftoff technique.

An effective way to influence the transport behavior is to apply an annealing step after the nanopatterning. We used an annealing temperature of 150 °C and durations from 30 min to 3 h. The post patterning annealing removes probably some of the defects induced by chemically assisted ion-beam etching. This can change an initially insulating sample to one in which Coulomb effects prevail or even to a conducting one. Annealing before the nanopatterning [11,18], which removes defects induced during low-temperature molecular beam epitaxy growth, is less effective than the post patterning annealing. Hence, the intrinsic structure of the NC is dominated by defects induced during the nanopatterning rather than by defects stemming from the low-temperature molecular beam epitaxy growth.

III. MEASUREMENT SETUP

All low-temperature measurements presented in this work were carried out at a temperature of about 25 mK using a ^{3}He/^{4}He-dilution fridge, equipped with a superconducting coil magnet. In combination with a rotatable sample holder, we were able to apply magnetic fields up to 19 T in any direction parallel to the sample plane. In order to saturate the magnetization of the device and to fix its direction, we applied a constant in-plane magnetic field with a magnitude of 1 T along one of the easy axes of the extended (Ga,Mn)As layer. This leads to a situation as sketched in Fig. 5(a). The electrical transport experiments were carried out in a two-terminal setup. We performed ac and dc measurements simultaneously by applying a dc bias voltage V_{dc} modulated with a small oscillating ac component V_{ac}. The current I flowing through the device was measured using a current amplifier which also converts the current into a corresponding voltage signal. The dc measurement using a digital multimeter provides the well-known I-V_{dc} characteristic, while the ac measurement using a lock-in amplifier offers the differential conductance $G = dI/dV_{ac}$ of the device. Our device could be tuned additionally by an external dc voltage (V_g) applied to the top-gate electrode of the device.

IV. EXPERIMENTAL RESULTS

A. Room-temperature properties

As mentioned in the Introduction, all nanoconstricted (Ga,Mn)As devices investigated in previous studies have

shown a rather complex and irregular Coulomb diamond pattern [10,11]. This has been explained by assuming that several metallic islands are involved in transport across the NC. Hence, shrinking the size of the NC should reduce the number of islands within the NC and bring up a more regular Coulomb diamond pattern. Looking for such samples, we investigated many different devices with widths and lengths of the NC ranging from 10 to 100 nm. Our experiments revealed that the transport properties of these devices are very sensitive to the width w of the NC while its length L has only a minor influence. Wider samples ($w > 25$ nm) show a mainly Ohmic behavior while the most narrow ones ($w < 15$ nm) are fully insulating. Only samples with intermediate widths of 15–25 nm show the typical SET-like behavior, discussed in the following. In many cases, the room-temperature resistance R_{NC} of the nanocontact already indicates whether the constriction is insulating, in the Coulomb-blockade regime, or Ohmic: For R_{NC}/R_s values (with the sheet resistance of $R_s \sim 4\,k\Omega$ at 4.2 K) between 10 and 15 the constriction was in most cases in the Coulomb-blockade regime for this specific material (see also Appendix A 2). However, similar to the earlier experiments, all of our SET-like samples, even the shortest and narrowest ones, have shown, on a first glance, an irregular Coulomb diamond pattern. Following, we discuss in more detail transport in the Coulomb-blockade regime.

B. Coulomb-blockade regime

In Fig. 2, we present a highly resolved stability diagram of one of our NC devices in the SET regime. The first impression is that the Coulomb diamond pattern is very irregular and exhibits frequent vertical discontinuities. Three of them are highlighted by white lines. These abrupt shifts can be assigned to charging or discharging of local traps in close vicinity to the NC, which, with their electrostatic potential, act as local gates. Their effect can thus be described as an abrupt jump along the gate voltage axis. This observation suggests a method to reconstruct the stability diagrams with unperturbed Coulomb diamonds. We cut the data set in Fig. 2 along the white lines and shift the segments on the V_g axis until the diamonds fit onto each other. An example of this procedure is shown in the top inset of Fig. 2. In this way we obtain, for some parts of the V_g scale, Coulomb diamonds which are essentially cleared of potential jumps due to charge fluctuations in local traps. The data set displayed in Fig. 3 has been reconstructed from the data shown in Fig. 2 and represents the starting point of our more detailed analysis.

The stability diagram shown in Fig. 3 presents characteristic features typical for metallic single-electron transistors [12–16] but also several anomalies. As expected, a series of diamonds

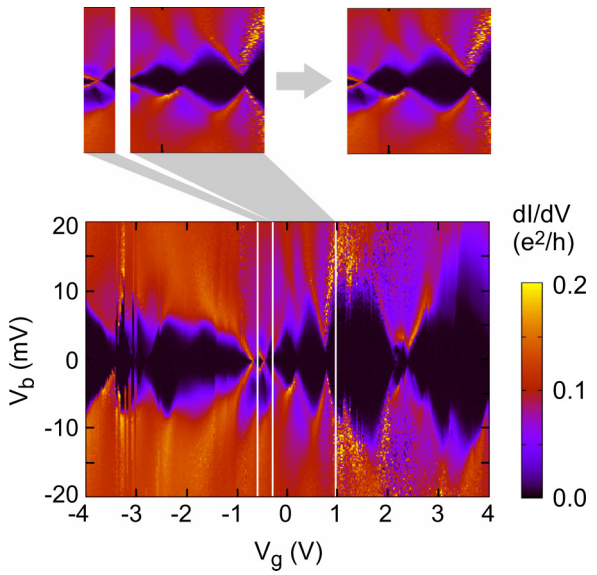

FIG. 2. (Color online) Differential conductance as a function of the bias and gate voltage of the NC device in Fig. 1. The measurement was done at a temperature of $T = 25$ mK. A partial irregular Coulomb diamond pattern with frequently occurring vertical discontinuities is observed. Three of those discontinuities are marked by white lines. Cutting the data set between two of these lines gives an undisturbed segment; stitching neighboring segments together as described in the text and shown in the upper inset allows to reconstruct the Coulomb diamond spectrum over a larger gate voltage range.

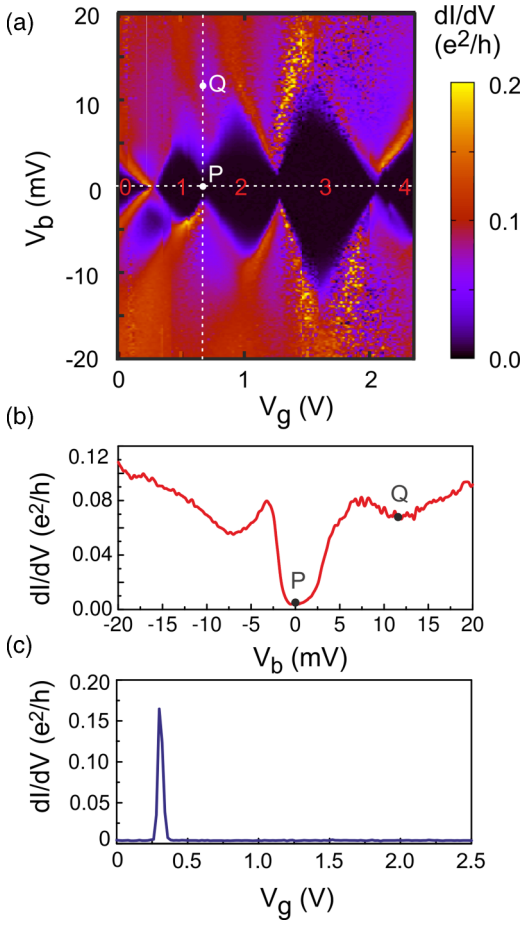

FIG. 3. (Color online) (a) Differential conductance of the NC device of Fig. 2 vs applied gate and bias voltages after reconstruction. Diamonds labeled 0 to 4 can clearly be identified. (b) Differential conductance as a function of the bias voltage corresponding to the vertical dashed line in (a). (c) Conductance at $V_b = 0$ as a function of the gate voltage corresponding to the horizontal dashed line in (a). It shows a conductance peak at the 0-1, and a blockade at the other charge degeneracy points, including point P.

of exponentially low differential conductance (black regions with fixed particle number) are surrounded by ridges of high conductance. Moreover, by further increasing the bias, the differential conductance does not drop to zero [see e.g. Fig. 3(b)], allowing to exclude the single-particle energy quantization typical for quantum dots. Unexpectedly, though, (i) the size and the shape of the Coulomb diamonds is not regular, (ii) some of the diamonds are not closing at zero bias [e.g., corners between diamonds 1 and 2 or between diamonds 2 and 3 as seen from the gate trace in Fig. 3(c)].

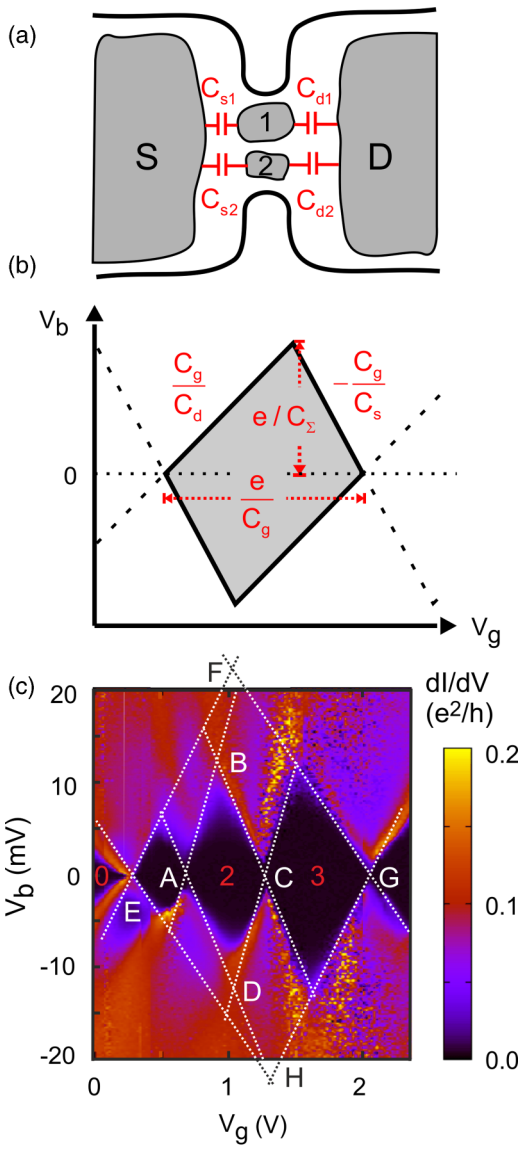

FIG. 4. (Color online) (a) Schematic of a double-island structure in a parallel configuration. Transport from source to drain is carried by two subsequent direct tunneling processes involving only one of the islands. The two islands are characterized by a different capacitive coupling to the leads (C_{si},C_{di}) as well as by a different gate capacitance (C_{gi}) with $i = 1,2$. (b) Schematic to illustrate the parameter extraction from a regular Coulomb diamond in the framework of the orthodox model. (c) The two Coulomb diamonds (ABCD and EFGH) used to extract the parameters are marked by white dotted lines.

Concerning the first anomaly, it is striking that all the diamonds exhibit an individual height as well as an individual width. Additionally the diamond labeled 1 and the diamond labeled 3 are asymmetric: according to the classical orthodox theory [12], one would expect that all Coulomb diamonds associated to a single island have the same size and shape, and that opposing edges of a Coulomb diamond were parallel. In the orthodox picture, the two different slopes of a Coulomb diamond are related to the capacitive coupling of the island to the source (C_s) and drain leads (C_d), as well as to the gate electrode (C_g). Assuming $C_g \ll C_{s,d}$, the slope of the source line is given by C_g/C_d while the slope of the drain line is given by $-C_g/C_s$ (see Fig. 4). In our case, only the diamond numbered 2 has parallel source and drain lines. The diamonds labeled 1 and 3, however, exhibit four different slopes, so that we would extract from each two different values for C_s and C_d or two different values for C_g, respectively. This suggests that our NC consists of at least two metallic islands producing a set of nested diamonds. In the following, we restrict ourselves to a double-island structure.

Figure 4(a) shows a simple schematic to illustrate our interpretation: the two islands are arranged in parallel, so that an electron can tunnel from the source lead directly to each of the two islands and from there in a subsequent tunneling process directly to the drain lead. By taking into account the slopes of the diamond edges as well as the distance between neighboring charge degeneracy points, we can obtain two different sets of parameters (C_s, C_d, C_g) from our experimental data. Each set of parameters characterizes one of the two islands. One set can be extracted from the regularly shaped diamond 2. For the other one, we have to reconstruct a second regular Coulomb diamond by extending the outer edges of diamonds 1 and 3 until they cross each other [see Fig. 4(c)]. The extracted parameters are summarized in Table I. Our analysis is limited to certain gate voltage ranges. We attribute this limitation to possible differences in the shape and even in the number of participating islands associated to different gate voltage regions. Nevertheless, the simple orthodox model gives already a satisfactory agreement between experimental and theoretical dI/dV_b stability diagrams and suggests that transport, in this gate voltage range, occurs primarily in parallel across two islands of different size in the reconstructed gate voltage segments. However, the model presented so far can not account for the second anomaly, i.e., a pronounced transport blocking observed in the vicinity of the charge degeneracy point between the diamonds 1-2 and 2-3 [see also Fig. 2(b)]. On

TABLE I. Parameters for the small and large Coulomb diamonds (CD) extracted from Fig. 3(a) assuming a double-island structure in the framework of the orthodox theory. The charging energy $U = e^2/C_\Sigma$, with $C_\Sigma = C_s + C_d + C_g$ being the total capacitance, is also given for reference.

	Small CD (ABCD)	Large CD (EFGH)
C_d	5.6×10^{-18} F	3.0×10^{-18} F
C_s	8.4×10^{-18} F	4.2×10^{-18} F
C_g	28×10^{-20} F	9×10^{-20} F
U	11.2×10^{-3} eV	21.9×10^{-3} eV

the other hand, the gap is not present at the charge degeneracy point 0-1 and is barely visible at 3-4 [see also Fig. 3(c)]. Hence, the gap is assigned to the island with the smaller charging energy. In order to account for this experimental observation, we resort below to a minimal transport model that includes the ferromagnetic nature of the material and provides a possible mechanism for the observed distinct blockade behavior.

V. THEORETICAL MODELING

In this section, we extend the orthodox theory of Coulomb blockade [12–16] in order to account for the ferromagnetic properties of the (Ga,Mn)As samples. Although transport through magnetic islands has been addressed in the literature [17], scarce consideration has been given, to our knowledge, to the role played by an energy-dependent density of states in the metallic islands. The latter, instead, is crucial to explain the anomalous current blocking observed in the present experiment.

To this end, we assume that both leads and the metallic islands are spin polarized. Figure 5(a) shows a sketch of the magnetization directions expected in the experiments. The magnetization of the ferromagnetic (Ga,Mn)As leads is rather weak, and can be tuned by an external magnetic field. It forms in our experiment an angle of 45° (easy direction) with the transport direction, set by the longitudinal axis of the NC [z axis, cf. Fig. 5(a)]. In the constriction, however, the spin polarization axis is strongly influenced by strain effects and is expected to be along the NC longitudinal axis.

In order to explain the blockade effects we claim that the angle θ between the leads and the constrictions magnetization lies in the range $\frac{1}{2}\pi < \theta < \frac{3}{2}\pi$. In other words, current

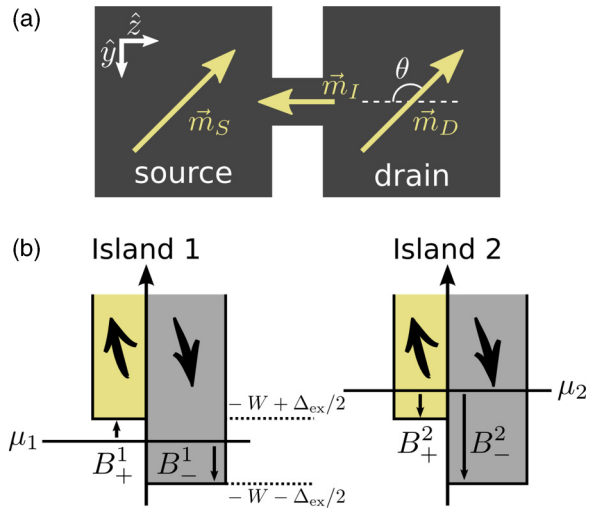

FIG. 5. (Color online) (a) Sketch of the magnetization direction of the leads ($\vec{m}_{S/D}$) and of the islands ($\vec{m}_I$). The magnetization of the leads is determined by the direction of the external magnetic field. In the constriction, on the other hand, strain effects are dominating and the magnetization direction lies parallel to the constriction axis. In our experiment, the angle between the two magnetizations is approximately $\theta = \frac{3}{4}\pi$. (b) Sketch of the density of states of the two metallic islands, with the spins aligned along the magnetization of the constriction.

suppression originates from the fact that the majority-spin carriers in the islands and in the leads have effectively the opposite polarization. Since only one of the two superimposed Coulomb diamond structures shows a noteworthy blockade effect, we conclude, within our model, that the structure with the blockade stems from transport through a fully polarized island, while the second island is only partially polarized.

We describe the islands' polarization with an upward shift in energy of the minority-spin band with respect to the majority-spin band [see Fig. 5(b)]. The electro-chemical potential is the external parameter which determines whether the island is partially or fully polarized. Partial polarization is obtained if the chemical potential μ_α ($\alpha = 1,2$) lies above the bottom of the minority-spin band, full polarization when the chemical potential lies between the bottom of the majority- and of the minority-spin bands.

In our model, the tunneling of a source electron of the majority-spin species (conventionally the spin up) to a fully down polarized island is highly suppressed for low-bias voltages since no spin-up states are available near the Fermi level. For bias voltages which are large enough to access also the minority-spin band [$\alpha_S e V_b > B^1_+$, cf. Fig. 5(b)], the suppression is lifted and an increase of the current is expected. For the partially polarized island, both spin species can be accessed already at the Fermi energy and no suppression is observed.

A. Model Hamiltonian

We describe the nanoconstriction with a system-bath model aimed at mimicking the structure of the two islands contacted to source and drain leads sketched in Fig. 4(a). The total Hamiltonian is

$$\hat{H} = \hat{H}_S + \hat{H}_T + \hat{H}_L, \tag{1}$$

where

$$\hat{H}_L = \sum_{\eta\in\{S,D\}} \sum_{k\sigma} E_{\eta k\sigma}\, \hat{c}^\dagger_{\eta k\sigma}\, \hat{c}_{\eta k\sigma} \tag{2}$$

denotes the Hamiltonian of the two spin polarized leads. We assume to have a flat, but spin-dependent, density of states ($\sigma = \uparrow / \downarrow$)

$$D_{\eta\uparrow} = \frac{1+p_\eta}{2} D_\eta, \quad D_{\eta\downarrow} = \frac{1-p_\eta}{2} D_\eta, \tag{3}$$

which depends on the polarization p_η of the leads ($-1 \leqslant p_\eta \leqslant 1$). The metallic islands ($\alpha \in \{1,2\}$) in the nanoconstriction are modeled by

$$\hat{H}_S = \sum_{\alpha\in\{1,2\}} \left\{ \sum_{i\tau} \epsilon_{\alpha i\tau}\, \hat{d}^\dagger_{\alpha i\tau}\, \hat{d}_{\alpha i\tau} + \alpha_g e V_g \hat{N}_\alpha + \frac{U_\alpha}{2} \hat{N}_\alpha (\hat{N}_\alpha - 1) \right\}, \tag{4}$$

and have in general a different spin quantization axis as the contacts. We define $\tau = \pm 1$ for spin $+/-$, respectively, using the spin-quantization axis of the nanoconstriction. As already mentioned, we account for the ferromagnetic properties of the metallic islands by assigning spin-dependent energy levels $\epsilon_{\alpha i\tau}$

and, consequently, a relative shift of the density of states for the two spin directions $\Delta_{\rm ex}$ [Fig. 5(b)]. The long-range Coulomb interactions are included within a constant interaction model, where U_α is the charging energy of the island α. The effective coupling of the gate electrode to the metallic islands is taken into account by the term proportional to $\alpha_{\rm g} e V_{\rm g}$, with $\alpha_{\rm g} = C_{\rm g}/C_\Sigma$ being an effective gate coupling parameter and $V_{\rm g}$ the gate voltage. The two metallic islands and the leads are weakly coupled by the tunneling Hamiltonian

$$\hat{H}_{\rm T} = \sum_{i\alpha\tau}\sum_{\eta k\sigma}[t_{\eta\alpha\sigma}u_{\sigma\tau}(\theta)\,\hat{\rm c}^\dagger_{\eta k\sigma}\,\hat{\rm d}_{\alpha i\tau} + {\rm H.c.}], \tag{5}$$

where we defined the function $u_{\uparrow+}(\theta) = u_{\downarrow-}(\theta) = \cos(\theta/2)$, $u_{\uparrow-}(\theta) = u_{\downarrow+}(\theta) = i\sin(\theta/2)$. It results from the noncollinear spin-quantization axes of the islands and the leads. Since the two axes are rotated by an angle of θ in the y-z plane with respect to each other, the transformation conserves the spin during tunneling.

B. Density of states of the metallic islands

Some of the experimental observations can only be understood if the energy dependence of the density of states, in particular the presence of different band edges for minority and majority spins, is accounted for. Specifically, we define the spin-dependent density of states of island α as

$$\begin{aligned} g_{\alpha\tau}(\epsilon) &= \tilde{g}_{\alpha\tau}\Theta(\epsilon + W - \tau\Delta_{\rm ex}/2)\Theta(W + \tau\Delta_{\rm ex}/2 - \epsilon) \\ &\approx \tilde{g}_{\alpha\tau} f^-(\epsilon + W - \tau\Delta_{\rm ex}/2), \end{aligned} \tag{6}$$

where W is the spin-independent contribution to the bandwidth, and $\Delta_{\rm ex}$ the exchange band splitting of the ferromagnetic metallic island. The parameter $\tilde{g}_{\alpha\tau}$ defines the strength of the density of states. Since the W is the largest energy scale considered in the following, the upper limit of the density of states can be set to infinity. In the last line of Eq. (6), we have approximated the left Heaviside function by $f^- = 1 - f^+$, with f^+ the Fermi function; this allows us to further proceed analytically in the calculation of the transport properties. The density of states is also sketched for clarity in Fig. 5(b). For later reference we define B^α_τ as the energy difference between the bottom of the band of the corresponding spin species τ and the chemical potential of the island α: $B^\alpha_\tau = -W + \tau\Delta_{\rm ex}/2 - \mu_\alpha$.

C. Transport theory

In the following, we briefly outline the main steps leading to the evaluation of the transport characteristics, emphasizing the new ingredients entering our transport theory. For more details, we refer to the Appendix B. The framework is the orthodox theory of Coulomb blockade [12–16], extended to the case of ferromagnetic contacts [17], and valid also for fully spin polarized metallic islands. The explicit derivation of the tunneling rates should illustrate the crucial role played in our theory by the energy-dependent density of states.

The theory is based on a master equation for the reduced density matrix of the islands, up to second order in the tunneling Hamiltonian. Since the two metallic islands are assumed not to interact with each other, the corresponding density matrices obey independent equations of motion (see Appendix B). Moreover, the metallic islands are assumed large enough to posses a quasicontinuous single-particle spectrum, but small enough that their charging energy dominates the tunneling processes that change their particle number. We further assume that, in-between two tunneling events, the islands relax to a local thermal equilibrium. Under these assumptions, the reduced density matrix of island α can be written as

$$\hat{\rho}^\alpha_{\rm red}(t) = \sum_{N_\alpha}\left\{\mathcal{P}_{N_\alpha}\frac{e^{-\beta\hat{H}_{{\rm S},\alpha}}}{\mathcal{Z}_{N_\alpha}}\right\}P_{N_\alpha}(t), \tag{7}$$

where $H_{{\rm S},\alpha}$ is the part of the system Hamiltonian associated to the island α, $\mathcal{P}_{N_\alpha}$ is the projection operator on the N_α-particle subspace, and $\mathcal{Z}_{N_\alpha} = {\rm Tr_S}(\mathcal{P}_{N_\alpha}e^{-\beta\hat{H}_{{\rm S},\alpha}})$ is the corresponding (canonical) partition function. By projecting the master equation on the N_α-particle subspace and tracing over the islands degrees of freedom, we keep only the occupation probabilities P_{N_α} of finding the island occupied by N_α electrons as dynamical variables. In the stationary limit, we find (see Appendix B)

$$\begin{aligned} {\rm Tr_S}\left\{\mathcal{P}_{N_\alpha}\dot{\hat{\rho}}^\alpha_\infty\right\} &= 0 \\ &= \sum_{\eta\sigma}\Big\{-\Gamma^{N_\alpha\to N_\alpha-1}_{\eta\alpha\sigma}P_{N_\alpha} - \Gamma^{N_\alpha\to N_\alpha+1}_{\eta\alpha\sigma}P_{N_\alpha} \\ &\quad + \Gamma^{N_\alpha-1\to N_\alpha}_{\eta\alpha\sigma}P_{N_\alpha-1} + \Gamma^{N_\alpha+1\to N_\alpha}_{\eta\alpha\sigma}P_{N_\alpha+1}\Big\}. \end{aligned} \tag{8}$$

Eventually, the stationary current through lead η reads as

$$I_\eta = -e\sum_{\alpha\sigma}\sum_{N_\alpha}\left\{\Gamma^{N_\alpha\to N_\alpha+1}_{\eta\alpha\sigma} - \Gamma^{N_\alpha\to N_\alpha-1}_{\eta\alpha\sigma}\right\}P_{N_\alpha}. \tag{9}$$

In Eqs. (8) and (9), the rates are defined as

$$\begin{aligned} \Gamma^{N_\alpha+1\to N_\alpha}_{\eta\alpha\sigma} &= \sum_\tau\frac{1+\sigma\,p_\eta}{2e^2R^{\eta\sigma}_{\alpha\tau}}|u_{\sigma\tau}(\theta)|^2 b^-\left(\Delta E^G_{N_\alpha} - \alpha_\eta e V_{\rm b}\right) \\ &\quad\times\left\{F\left(\Delta E^G_{N_\alpha} + B^\alpha_\tau - \alpha_\eta e V_{\rm b}\right) - F\left(B^\alpha_\tau\right)\right\}, \\ \Gamma^{N_\alpha\to N_\alpha+1}_{\eta\alpha\sigma} &= \sum_\tau\frac{1+\sigma\,p_\eta}{2e^2R^{\eta\sigma}_{\alpha\tau}}|u_{\sigma\tau}(\theta)|^2 b^+\left(\Delta E^G_{N_\alpha} - \alpha_\eta e V_{\rm b}\right) \\ &\quad\times\left\{F\left(B^\alpha_\tau\right) - F\left(\Delta E^G_{N_\alpha} + B^\alpha_\tau - \alpha_\eta e V_{\rm b}\right)\right\}, \end{aligned} \tag{10}$$

and are expressed in terms of the normal-state resistance $R^{\eta\sigma}_{\alpha\tau} = \hbar/(2\pi e^2|t_{\eta\alpha\sigma}|^2\tilde{g}_{\alpha\tau}D_\eta)$ and the functions $b^\pm(x) = 1/(e^{\pm\beta x} - 1)$ and $F(x) = x/(e^{\beta x} - 1)$, with $\beta = 1/(k_{\rm B}T)$ the inverse temperature. We account for the asymmetric bias drop with the bias coupling constants defined as $\alpha_{\rm S/D} = \pm\frac{C_{\rm d/s} + C_{\rm g}/2}{C_\Sigma}$. Further, we defined the grand canonical addition energy

$$\begin{aligned} \Delta E^G_{N_\alpha} &= \alpha_{\rm g} e V_{\rm g} + U_\alpha N_\alpha + \mu_\alpha - \mu_0 \\ &= \left[E_{N_\alpha+1} - \mu_0(N_\alpha+1)\right] - \left(E_{N_\alpha} - \mu_0 N_\alpha\right) \end{aligned} \tag{11}$$

which must be paid in order to increase the electron number on island α from $N_\alpha \to N_\alpha + 1$. We denote μ_0 the chemical potential of the leads at bias $V_{\rm b} = 0$.

The rates given in Eq. (10) differ from those of the orthodox theory of Coulomb blockade [12–16] even in their spin-dependent variation [17] due to the energy-dependent

density of states and the explicit dependence on the band edges. The latter introduce a new source of current suppression associated to the absence of states with a specific spin species. These rates represent the main theoretical contribution of this work. For the chemical potential lying far above the bottom of the bands, the theory recovers again the limit of the classical orthodox theory of Coulomb blockade. Namely, in the limit $B \to -\infty$,

$$\lim_{B\to-\infty} \pm b^{\pm}(x)\{F(B) - F(x+B)\} = F(\pm x). \qquad (12)$$

VI. THEORETICAL RESULTS

A. Comparison with the experiments

The results of our simulation are reported in Fig. 6(a), with the differential conductance shown as a function of the bias and gate voltage. We see the same nested diamond structure as in the experiments. In our theory, the diamonds at the charge degeneracy points labeled 0-1 and 3-4 close. Between the diamonds 1-2 and 2-3 the differential conductance is suppressed for bias voltages smaller than a certain threshold bias. Figure 6(b) shows a bias trace calculated at the charge degeneracy point 1-2, for two different angles θ between the magnetization vectors of the leads $\vec{m}_\alpha$ and the metallic islands $\vec{m}_I$. It shows a suppression of the differential conductance at point (P) with respect to point (Q). The width of the suppression region corresponds to the one observed experimentally in Fig. 3(b) and is proportional to B^1_+, the energy difference between the bottom of the minority-spin band and the chemical potential of island 1 [cf. Fig. 5(b)]. In contrast to the experiments, no full blockade can be observed at (P). A change of the orientation of the magnetization directions from $\theta = \pi$ (dashed red line) to $\theta = \frac{3}{4}\pi$ (solid blue line) is shifting the curve upwards. Aside from the constant shift, the two curves are qualitatively the same.

To emphasize the effect of the islands' degree of polarization on the suppression mechanism, a conductance trace at $V_b = 0$ of a full polarized island 1 is compared to the case of a partial polarized island 1 in Fig. 6(c). Partial polarization is achieved by shifting the electrochemical potential of island 1 by 12 meV up in energy. The solid blue line shows the full polarized case, where the two larger peaks correspond to the larger Coulomb diamond (island 2). The peak observed in the experiment [Fig. 3(c)] we ascribe to transport across this partially polarized island. Although the theoretically predicted second peak is missing in Fig. 3(c) we note that the corresponding blockade between diamonds 3 and 4 is much less pronounced than between, e.g., 2 and 3. This asymmetry between the degeneracy points 0-1 and 3-4, however, cannot be accounted for by our model which predicts a periodicity of the Coulomb oscillation pattern. The four smaller peaks in Fig. 6(c) belong to the smaller Coulomb diamond structure, corresponding to island 1, i.e., the fully polarized one [Fig. 5(b)]. Even though the conductance is not completely suppressed as in the experiment, the conductance peaks are strongly reduced with respect to the partially polarized case. In the latter (dashed gray lines), no suppression is present and the conductance peaks of island 1 are by a factor of 4 larger. In the following, we address a possible reason for the incomplete blocking within the model. Since the parameters of island 2 are kept the same, both for the fully and partially polarized

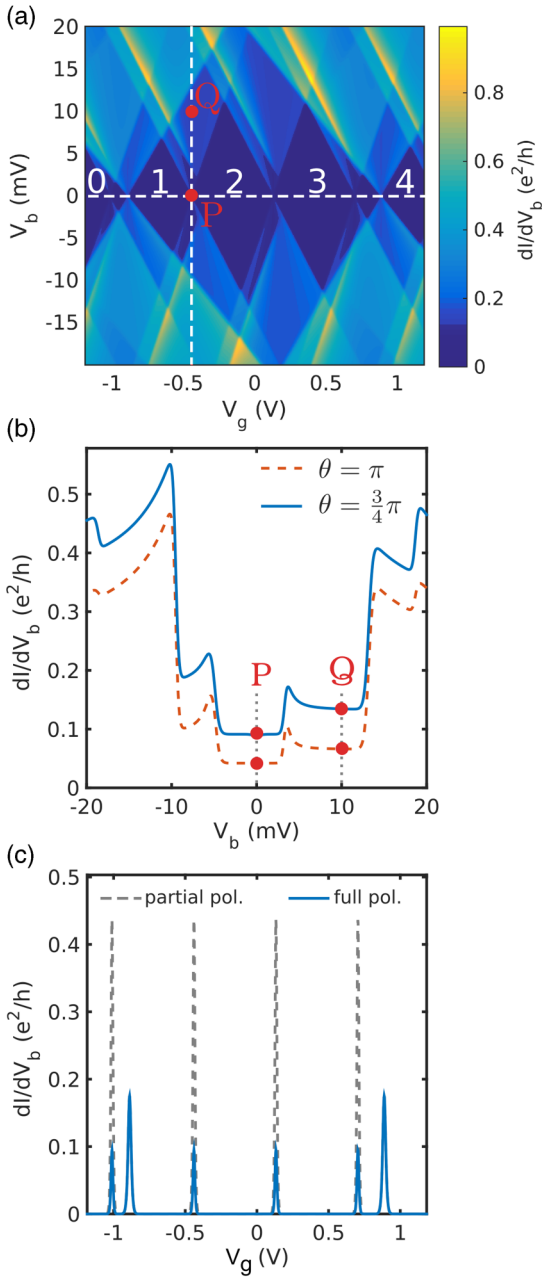

FIG. 6. (Color online) (a) Calculated differential conductance of two spin polarized metallic islands with spin polarized leads. The island with the larger charging energy is assumed to be partially polarized, while the island with the smaller charging energy is fully polarized. (b) Bias trace through a charge degeneracy point of the fully polarized island. The gate position of the line trace is marked as a dashed line in (a). (c) Gate traces at $V_b = 0$ for a full (solid blue line) and a partial polarization (dashed gray line) of island 1. Island 2 remains partially polarized. In the fully polarized case, the conductance peaks of island 1 are suppressed with respect to the partially polarized case. For island 2, both curves are identical. The parameters used to obtain this figure are $\alpha_{S1} = 0.4$, $\alpha_{S2} = 0.42$, $U_1 = 11.2$ meV, and $U_2 = 21.9$ meV in accordance with the parameters for the capacitive couplings of Table I. Moreover, $R^{\eta\sigma}_{1\tau} = 0.57 \times 10^3 h/e^2$, $R^{\eta\sigma}_{2\tau} = 1.4 \times 10^3 h/e^2$, $B^1_+ = 2$ meV, $B^1_- = -18$ meV, $B^2_+ = -10$ meV, $B^2_- = -35$ meV, $\mu_1 = -42$ meV, $\mu_2 = -32$ meV, $p_\eta = 0.8$, and $k_B T = 0.07$ meV. For the full polarized island 1 in (c) $B^1_+ = -10$ meV, $B^1_- = -30$ meV.

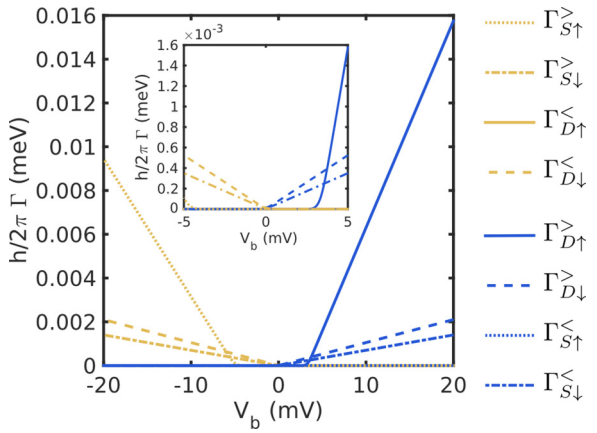

FIG. 7. (Color online) All tunneling rates for the island 1 plotted at a charge degeneracy point as a function of the bias voltage V_b. The angle between the two magnetization directions is $\theta = \pi$.

cases the corresponding conductance peaks are not changing. Despite the fact that a comparison of the calculated gate trace to the experimental one in Fig. 3(c) reveals some limitations of the model, the essential feature, i.e., the suppression inside the large Coulomb diamond, is reproduced.

B. Mechanism of current suppression

For a better understanding of the mechanism underlying the blockade, we derive analytically the differential conductance for the island 1 at the two points (P) and (Q) marked in Fig. 6(b). For simplicity, the case $\theta = \pi$ is considered since qualitatively the blockade mechanism is the same in both cases.

Notice that both P and Q correspond to a gate voltage such that $\Delta E_N^G = 0$, i.e., at the charge degeneracy point of the N-$N+1$ transition. To obtain the differential conductance, according to Eqs. (8) and (9), the transition rates $\Gamma_{\eta\alpha\sigma}^{N\to N\pm1}$ are required. For simplicity, we have dropped the subscript 1 from the excitation energy ΔE_N^G since we will refer from now on always to the same island.

In Fig. 7, we show the transition rates as a function of the bias V_b. To simplify the notation, we replaced $\Gamma_{\eta\alpha\sigma}^{N\to N\pm1} \to \Gamma_{\eta\sigma}^{\gtrless}$. Notice their linear dependence on the bias above a certain threshold. Thus, in that bias range one can approximate them as

$$\begin{aligned}\Gamma_{\mathrm{S}\downarrow}^{<} &= -\mathcal{B}_{\mathrm{S}\downarrow} V_b,\\ \Gamma_{\mathrm{D}\downarrow}^{>} &= \mathcal{B}_{\mathrm{D}\downarrow} V_b,\\ \Gamma_{\mathrm{D}\uparrow}^{>} &= \mathcal{A}_{\mathrm{D}\uparrow} + \mathcal{B}_{\mathrm{D}\uparrow} V_b,\end{aligned} \tag{13}$$

where $\mathcal{A}_{\mathrm{D}\uparrow}$ is a constant accounting for the threshold bias, and

$$\mathcal{B}_{\eta\sigma} = \frac{2\pi e}{\hbar^2} D_0 \frac{1+\sigma p}{2} \tilde{g}_\sigma \alpha_\eta |t_\eta|^2. \tag{14}$$

Here, $D_0 = D_\eta$ is assumed to be independent of the lead. For the point (P) within the first plateau only the rates with $\sigma = \downarrow$, namely $\Gamma_{\mathrm{D}\downarrow}^{>}$ and $\Gamma_{\mathrm{S}\downarrow}^{<}$, are nonzero. Hence, according to the principle of detailed balance $\Gamma_{\mathrm{D}\downarrow}^{>} P_N = \Gamma_{\mathrm{S}\downarrow}^{<} P_{N+1}$. Imposing probability conservation we find $P_N = \Gamma_{\mathrm{S}\downarrow}^{<}/(\Gamma_{\mathrm{D}\downarrow}^{>} + \Gamma_{\mathrm{S}\downarrow}^{<})$. Thus, the stationary current equals $I_D^{(P)} = -e\Gamma_{\mathrm{D}\downarrow}^{>} P_N = -e\Gamma_{\mathrm{D}\downarrow}^{>}\Gamma_{\mathrm{S}\downarrow}^{<}/(\Gamma_{\mathrm{D}\downarrow}^{>} + \Gamma_{\mathrm{S}\downarrow}^{<}) \propto (1-p)^2$, which is suppressed for a large spin polarization p. Here, the polarization p is assumed to be equal for both leads.

At the point (Q), only one additional rate $\Gamma_{\mathrm{D}\uparrow}^{>}$ is contributing (the rate $\Gamma_{S\uparrow}^{<}$ is zero due to the lower bound of the density of states). In this bias range, the equations of detailed balance and probability conservation yield $P_N = \Gamma_{\mathrm{S}\downarrow}^{<}/(\Gamma_{\mathrm{D}\downarrow}^{>} + \Gamma_{\mathrm{D}\uparrow}^{>} + \Gamma_{\mathrm{S}\downarrow}^{<})$. The resulting stationary current is then $I_D^{(Q)} = -e(\Gamma_{\mathrm{D}\downarrow}^{>} + \Gamma_{\mathrm{D}\uparrow}^{>})P_N = -e(\Gamma_{\mathrm{D}\downarrow}^{>} + \Gamma_{\mathrm{D}\uparrow}^{>})\Gamma_{\mathrm{S}\downarrow}^{<}/(\Gamma_{\mathrm{D}\downarrow}^{>} + \Gamma_{\mathrm{D}\uparrow}^{>} + \Gamma_{\mathrm{S}\downarrow}^{<}) \propto (1-p)$. Again, the current is suppressed for large spin polarization.

Inserting Eq. (13) into the current expressions at the points P and Q, we find

$$I_D^{(\mathrm{P})} = e\frac{\mathcal{B}_{\mathrm{S}\downarrow}\mathcal{B}_{\mathrm{D}\downarrow}}{\mathcal{B}_{\mathrm{D}\downarrow} - \mathcal{B}_{\mathrm{S}\downarrow}} V_b \tag{15}$$

and

$$I_D^{(\mathrm{Q})} = e\frac{+\mathcal{B}_{\mathrm{S}\downarrow}\mathcal{A}_{\mathrm{D}\uparrow} V_b - \mathcal{B}_{\mathrm{S}\downarrow}(\mathcal{B}_{\mathrm{D}\uparrow} + \mathcal{B}_{\mathrm{D}\downarrow})V_b^2}{\mathcal{A}_{\mathrm{D}\uparrow} + (\mathcal{B}_{\mathrm{D}\uparrow} + \mathcal{B}_{\mathrm{D}\downarrow} - \mathcal{B}_{\mathrm{S}\downarrow})V_b}. \tag{16}$$

Taking the ratio of the two differential conductance plateaus, i.e., the ratio of Eqs. (D1) and (D2), we find

$$\begin{aligned}&\frac{dI_D^{(\mathrm{P})}}{dV_b} \Big/ \frac{dI_D^{(\mathrm{Q})}}{dV_b}\\ &= \frac{1}{\alpha_D|t_\mathrm{D}|^2 - \alpha_\mathrm{S}|t_\mathrm{S}|^2}\\ &\quad\times\left(\alpha_D|t_\mathrm{D}|^2 - \alpha_\mathrm{S}|t_\mathrm{S}|^2\frac{(1-p)\tilde{g}_\downarrow}{(1+p)\tilde{g}_\uparrow + (1-p)\tilde{g}_\downarrow}\right).\end{aligned} \tag{17}$$

Thus, within our simple model, the ratio $\mathcal{R}$ of the height of the two plateaus is limited by

$$\frac{\alpha_D|t_\mathrm{S}|^2}{\alpha_D|t_\mathrm{D}|^2 - \alpha_\mathrm{S}|t_\mathrm{S}|^2} \leqslant \mathcal{R} \leqslant 1. \tag{18}$$

In other words, the ratio of the two differential conductance plateaus is limited in our theory, leading to some discrepancy with the experimentally observed ratio [cf. points P and Q marked in Fig. 3(b)]. Since the parameters α_η are determined experimentally, the only possibility to change the ratio is to modify the coupling constants $|t_\eta|$. However, the increase of the coupling constants necessary to fit the experimental value would lead to a huge asymmetry in the stability diagram which is not observed experimentally. Despite the discrepancy between $\mathcal{R}$ and the experimental ratio, we think that the theory clearly suggests a mechanism which can lead to a suppression of the conductance due to spin polarization in the framework of an orthodox theory of Coulomb blockade. To better fit the experiments, a more realistic energy dependence of the density of states which also accounts for valence bands is necessary. With such an energy dependence, the rates can change their slope as a function of the bias voltage, leading to an even more pronounced bias-dependent suppression of the differential conductance.

VII. CONCLUSION

In this work, we have reported on a detailed study of the transport characteristics of nanofabricated narrow constrictions in (Ga,Mn)As thin films. By means of a two-step electron

beam lithography technique we have fabricated well-defined nanoconstrictions of different sizes. Depending on channel width and length, for a specific material, different low-temperature transport regimes have been identified, namely, the Ohmic regime, the single-electron tunneling regime (SET), and a completely insulating regime. In the SET, complex stability diagrams with nested Coulomb diamonds and anomalous conductance suppression in the vicinity of charge degeneracy points have been measured.

In order to rationalize these observations, we proposed, for a specific nanoconstriction, a model consisting of two ferromagnetic islands coupled to ferromagnetic leads. In particular, the angle θ between the leads and the islands magnetization lies in the range $\frac{1}{2}\pi < \theta < \frac{3}{2}\pi$. Moreover, the full polarization of one of the metallic islands is crucial. The data do not conclusively support a two-island model and we can not exclude a more complex island structure. We studied the transport characteristics of the system in terms of a modified orthodox theory of Coulomb blockade which takes into account the energy dependence of the density of states in the metallic islands. The latter represents an important generalization of existing formulations and is determinant for the qualitative understanding of the present experiments. In fact, the explicit appearance of the minority-spin band edge in the expression of the tunneling rates yields a pronounced conductance suppression at the charge degeneracy points. To account for the full suppression of conductance observed in the experiments, the simple model used in this work should be further improved. For example, the hole character of the charge carriers and associated spin-orbit coupling effects are not captured by our model. Furthermore, it is straightforward to combine the present theory with microscopic models that allow for a realistic description of the islands density of states.

ACKNOWLEDGMENT

We acknowledge for this work the financial support of the Deutsche Forschungsgemeinschaft under the research programs SFB 631 and SFB 689.

APPENDIX A: EXPERIMENTAL DETAILS

1. Sample fabrication: Two-step EBL fabrication process

Both steps are based on the standard EBL resist polymethyl-methacrylate (PMMA). In the first step, one exposes the resist using an extremely high line dose (approximately 3×10^4 pC/cm) in order to define a narrow crosslinked PMMA line. This line is very robust and does not get removed by common organic solvents like acetone. Hence, after cleaning the sample in a bath of acetone, the crosslinked PMMA line remains on top of the sample while the unexposed PMMA is removed from the sample surface. For the second step, the sample is again coated with a fresh layer of PMMA resist. This time one uses a common dose (approximately 2000 pC/cm) in order to expose a second line perpendicular to the crosslinked one. After removing the exposed resist using a standard developer solution consisting of isopropyl alcohol and methyl-isobutyl-ketone (MIBK), we get the patterned mask for the subsequent ion-beam etching, shown in Fig. 1(a).

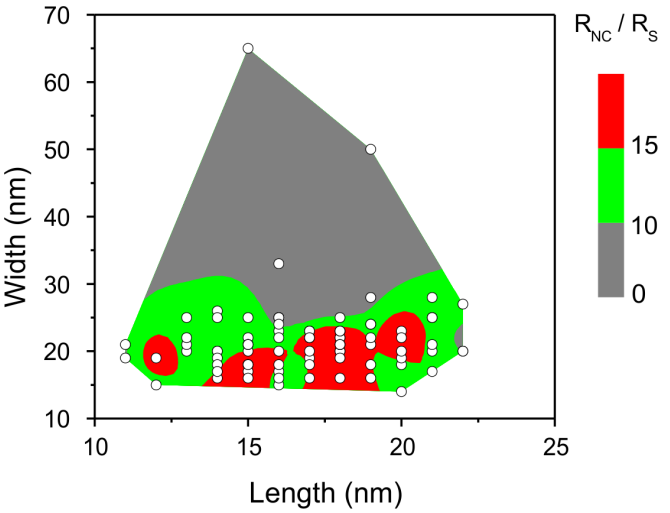

FIG. 8. (Color online) Open circles show various NC devices having different length and width fabricated from the material used in experiment. Their corresponding room-temperature resistance, normalized to the sheet resistance $R_s = 4$ kΩ of the (Ga,Mn)As layer, is color coded and sorted into three classes. At low temperatures, devices with $R_{NC}/R_s > 15$ were in most cases found to be fully insulating, samples with R_{NC}/R_s between 10 and 15 showed Coulomb blockade, while nanocontacts with a relative resistance smaller than 10 displayed an essential linear I-V characteristic.

2. Size dependence of the transport characteristics

As mentioned in Sec. IV A, the transport characteristics of the samples crucially depend on the dimensions of the nanoconstriction. Figure 8 relates the transport behavior of the devices to the dimensions of the constriction. In particular, it shows room-temperature measurements of the devices' resistance normalized to the sheet resistance of $R_s = 4$ kΩ, as a function of the constrictions width and length. The white circles represent measurements of different samples. Their transport behavior is schematically illustrated by the background color, while devices in the red areas were predominantly insulating, the ones in the green areas showed in most cases SET-like behavior, whereas in the gray areas Ohmic behavior prevails. A discussion about the dependence of the transport behavior on the constriction size is already given in Sec. IV A and is confirmed by Fig. 8.

The devices shown in Fig. 8 were measured at room temperature directly after sample fabrication without additional annealing steps applied to the sample and before the first cooldown. Aside from the contact size, additional annealing steps can drastically alter the transport regime. As mentioned in the main text, this can change an initially insulating sample to one in which SET effects prevail or even to a conducting one. Figure 9(a) displays the stability diagram of another device before annealing which is in the Coulomb-blockade regime. After annealing, a similar device (the original one broke), displayed in Fig. 9(b), shows no Coulomb blockade at all, but essentially linear behavior.

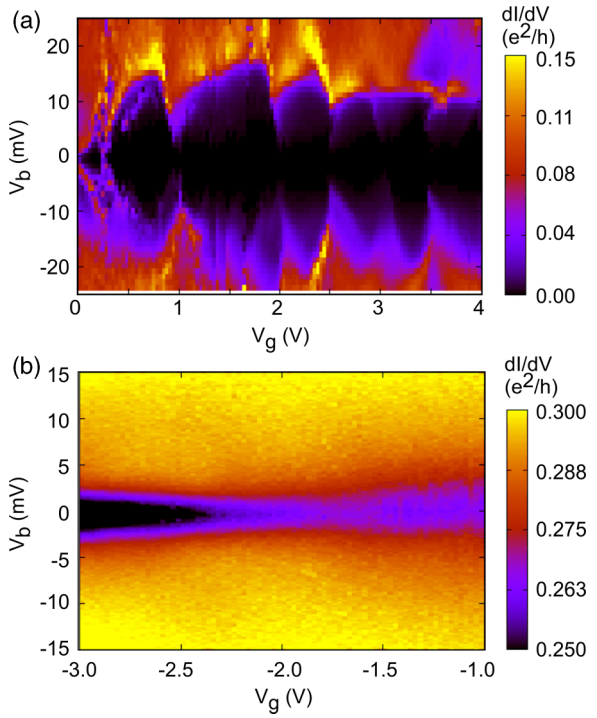

FIG. 9. (Color online) (a) A device with length/width of 16/15 nm before annealing and with $R_{NC}/R_s \sim 12.15$ at room temperature shows pronounced SET behavior. (b) Another device with similar $R_{NC}/R_s \sim 12$ shows after annealing at 150 °C for 3 h nearly Ohmic behavior.

3. Angular dependence of the transport characteristic

Figure 10 displays differential conductance stability diagrams, measured for different directions of the magnetic field for the device discussed in the main text. As already discussed there, the data exhibit frequent vertical discontinuities. Hence, conclusions about the magnetic field dependence of the measurements can be drawn only in undisturbed gate voltage regions. The white arrows in Fig. 10 mark the position of two characteristic features in all subfigures. One clearly sees that the Coulomb-blockade threshold marked by (1) is shrinking towards lower bias voltages by rotating the magnetic field direction. A similar behavior is observed at position (2). This strong dependence on the magnetic field directions reflects the anisotropy, typical in these systems [6,10].

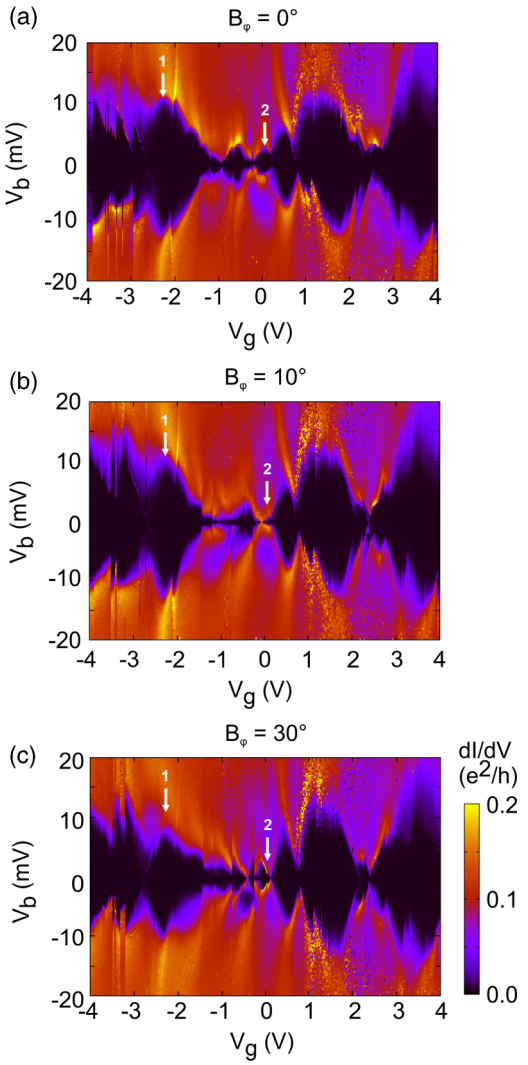

FIG. 10. (Color online) Differential conductance stability diagrams of the sample discussed in the main text measured for different directions of the magnetic field. The field strength was in all cases 1 T, the temperature 25 mK. Arrows in (a) mark the tip of two diamonds. Their V_g position is kept fixed in (b) and (c) showing that the direction of the magnetic field changes Coulomb blockade.

APPENDIX B: EQUATION OF MOTION FOR A ORTHODOX THEORY OF COULOMB BLOCKADE

In this Appendix, we derive an extension of the orthodox theory of Coulomb blockade for the case of spin polarized contacts as well as of a spin polarized metallic island. In particular, we will consider explicitly the lower bound of the density of states in the metallic island.

The transport theory is based on the Liouville–von Neumann equation for the reduced density matrix in the interaction picture

$$i\hbar\frac{\partial}{\partial t}\hat{\rho}_{\mathrm{I}}(t) = [\hat{H}_{\mathrm{T,I}}(t), \hat{\rho}_{\mathrm{I}}(t)], \tag{B1}$$

which we expand to second order in the tunneling Hamiltonian $\hat{H}_{\mathrm{T}}$. Prior to $t = 0$ the system and the leads do not interact and the density matrix can be written as a tensor product of the density matrices of the subsystems

$$\hat{\rho} = \hat{\rho}_S(0) \otimes \hat{\rho}_{\mathrm{L}} \equiv \hat{\rho}_{\mathrm{S}}(0)\hat{\rho}_{\mathrm{L}}. \tag{B2}$$

Since the leads are considered thermal baths of noninteracting fermions, $\hat{\rho}_{\mathrm{L}}$ reads as

$$\hat{\rho}_{\mathrm{L}} = \frac{e^{-\beta(\hat{H}_{\mathrm{L}} - \sum_\eta \mu_\eta \hat{N}_\eta)}}{\mathcal{Z}_{\mathrm{L,G}}}. \tag{B3}$$

Further, we assume that due to fast relaxation processes in the leads, the density matrix can be written as $\hat{\rho}_{\mathrm{I}}(t) = \hat{\rho}_{\mathrm{red,I}}(t)\hat{\rho}_{\mathrm{L}} + \mathcal{O}(\hat{H}_{\mathrm{T}})$, with $\hat{\rho}_{\mathrm{red,I}} = \mathrm{Tr}_{\mathrm{L}}\hat{\rho}$. Moreover, due to the independence of the two metallic islands $\hat{\rho}_{\mathrm{red}}(t) = \hat{\rho}^1_{\mathrm{red}}(t)\hat{\rho}^2_{\mathrm{red}}(t)$ and each

component obeys the following equation of motion:

$$\dot{\hat{\rho}}^{\alpha}_{\rm red}(t) = -\frac{i}{\hbar}\big[\hat{H}_{\rm S}, \hat{\rho}^{\alpha}_{\rm red}(t)\big] - \frac{1}{\hbar^2}\int_0^t dt''\,{\rm Tr}_{\rm L}\left\{\big[\hat{H}_{\rm T}, \big[H_{\rm T,I}(-t''), \hat{\rho}^{\alpha}_{\rm red}(t)\rho_L\big]\big]\right\}, \tag{B4}$$

where $\alpha = 1,2$ labels the metallic island.

For the system we assume that the metallic islands are large enough to possess a quasicontinuous single-particle spectrum, but small enough that their charging energy dominates the tunneling processes that change their particle number. Furthermore, it is assumed that the islands will relax to a local thermal equilibrium on a time scale shorter than the inverse of the average electronic tunneling rate. Under these assumptions, the reduced density matrix can be written as

$$\hat{\rho}^{\alpha}_{\rm red}(t) = \sum_{N_\alpha} \mathcal{P}_{N_\alpha} \frac{e^{-\beta \hat{H}_{{\rm S},\alpha}}}{\mathcal{Z}_{N_\alpha}} P_{N_\alpha}(t), \tag{B5}$$

with $\mathcal{Z}_{N_\alpha} = {\rm Tr}_{\rm S}\{\mathcal{P}_{N_\alpha} e^{-\beta \hat{H}_{{\rm S},\alpha}}\}$, and

$$\mathcal{P}_{N_\alpha} = \sum_{\substack{\{n_i\}_\alpha \\ \sum_i n_i = N_\alpha}} |\{n_i\}_\alpha\rangle\langle\{n_i\}_\alpha| \tag{B6}$$

is the projection operator on the N_α-particle subspace. Notice that in Eq. (B5), due to the projector operator $\mathcal{P}_{N_\alpha}$, the only statistically relevant term of the system Hamiltonian $\hat{H}_{{\rm S},\alpha}$ is $\hat{h}^{\alpha}_{\rm S} = \sum_{i\sigma} \epsilon_{\alpha i\sigma} d^{\dagger}_{\alpha i\sigma} d_{\alpha i\sigma}$. The term $e^{-\beta[\frac{U_\alpha}{2} N_\alpha(N_\alpha-1)+\alpha_{\rm g} e V_{\rm g} N_\alpha]}$ becomes a constant and is canceling out in the density matrix. Inserting explicitly $\hat{H}_{\rm T}$ in Eq. (B4), we find

$$\begin{aligned}
{\rm Tr}_{\rm S}\left\{\mathcal{P}_{N_\alpha}\dot{\hat{\rho}}^{\alpha}_{\rm red}(t)\right\} = -\frac{1}{\hbar^2}\sum_{\eta\eta'}\sum_{\substack{ki\sigma\tau \\ k'i'\sigma'\tau'}} t_{\eta\alpha\sigma} u_{\sigma\tau}(\theta) t^{*}_{\eta'\alpha\sigma'} u^{*}_{\sigma'\tau'}(\theta) \int_0^t dt''\Big\{ &{\rm Tr}_{\rm S}\left\{\mathcal{P}_{N_\alpha}\,\hat{\rm d}^{\dagger}_{\alpha i\tau}\,\hat{\rm d}_{\alpha i'\tau',I}(-t'')\hat{\rho}^{\alpha}_{\rm red}(t)\right\} \\
&\times {\rm Tr}_{\rm L}\{\hat{\rm c}_{\eta k\sigma}\,\hat{\rm c}^{\dagger}_{\eta' k'\sigma',{\rm I}}(-t'')\hat{\rho}_{\rm L}\} + {\rm Tr}_{\rm S}\left\{\mathcal{P}_{N_\alpha}\,\hat{\rm d}_{\alpha i\tau}\,\hat{\rm d}^{\dagger}_{\alpha i'\tau',{\rm I}}(-t'')\hat{\rho}^{\alpha}_{\rm red}(t)\right\}{\rm Tr}_{\rm L}\{\hat{\rm c}^{\dagger}_{\eta k\sigma}\,\hat{\rm c}_{\eta' k'\sigma',{\rm I}}(-t'')\hat{\rho}_{\rm L}\} \\
&- {\rm Tr}_{\rm S}\left\{\hat{\rm d}_{\alpha i'\tau',{\rm I}}(-t'')\mathcal{P}_{N_\alpha}\,\hat{\rm d}^{\dagger}_{\alpha i\tau}\;\rho^{\alpha}_{\rm red}(t)\right\}{\rm Tr}_{\rm L}\left\{\,\hat{\rm c}^{\dagger}_{\eta' k'\sigma',{\rm I}}(-t'')\,\hat{\rm c}_{\eta k\sigma}\;\hat{\rho}_{\rm L}\,\right\} \\
&- {\rm Tr}_{\rm S}\left\{\hat{\rm d}^{\dagger}_{\alpha i'\tau'},{\rm I}(-t'')\mathcal{P}_{N_\alpha}\,\hat{\rm d}_{\alpha i\tau}\;\hat{\rho}^{\alpha}_{\rm red}(t)\right\}{\rm Tr}_{\rm L}\{\hat{\rm c}_{\eta' k'\sigma',{\rm I}}(-t'')\,\hat{\rm c}^{\dagger}_{\eta k\sigma}\;\hat{\rho}_{\rm L}\,\} + {\rm c.c.}\Big\}.
\end{aligned} \tag{B7}$$

In the following, we are analyzing the first term of Eq. (B7) in more detail, the other terms can be evaluated in complete analogy. The calculation of the trace over the lead degrees of freedom gives

$${\rm Tr}_{\rm L}\{\hat{\rm c}_{\eta k\sigma}\,\hat{\rm c}^{\dagger}_{\eta' k'\sigma',{\rm I}}(-t'')\hat{\rho}_{\rm L}\} = e^{\frac{i}{\hbar}E_{\eta k}(-t'')} f^{-}(E_{\eta k}-\mu_\eta)\delta_{kk'}\delta_{\eta\eta'}\delta_{\sigma\sigma'}, \tag{B8}$$

where the time evolution of the creation and annihilation operators of the leads is given by $\hat{\rm c}^{\dagger}_{\eta k\sigma,{\rm I}}(t) = e^{\frac{i}{\hbar}E_{\eta k}t}\,\hat{\rm c}^{\dagger}_{\eta k\sigma}$. For the system operators, the time evolution can be carried out in a similar way, keeping in mind that the parts proportional to the total number operator can be factorized

$${\rm Tr}_{\rm S}\left\{\mathcal{P}_{N_\alpha}\,\hat{\rm d}^{\dagger}_{\alpha i\tau}\,\hat{\rm d}_{\alpha i'\tau',{\rm I}}(-t'')\hat{\rho}^{\alpha}_{\rm red}(t)\right\} = e^{\frac{i}{\hbar}[\epsilon_{\alpha i'\sigma'}+\alpha_{\rm g}eV_{\rm g}+U(N_\alpha-1)]t''}\,{\rm Tr}_{\rm S}\left\{\mathcal{P}_{N_\alpha}\,\hat{\rm d}^{\dagger}_{\alpha i\tau}\,\hat{\rm d}_{\alpha i'\tau'}\,\hat{\rho}^{\alpha}_{\rm red}(t)\right\}. \tag{B9}$$

In order to perform the trace over the system degrees of freedom, another approximation is necessary. By taking the average in the grand canonical ensemble, the particle number is determined by the chemical potential and we can remove the projection operator:

$${\rm Tr}_{\rm S}\left\{\mathcal{P}_{N_\alpha}\,\hat{\rm d}^{\dagger}_{\alpha i\sigma}\,\hat{\rm d}_{\alpha i'\sigma',{\rm I}}(-t'')\hat{\rho}^{\alpha}_{\rm red}(t)\right\} = {\rm Tr}_{\rm S}\left\{\mathcal{P}_{N_\alpha}\,\hat{\rm d}^{\dagger}_{\alpha i\sigma}\,\hat{\rm d}_{\alpha i'\sigma',{\rm I}}(-t'')\frac{e^{-\beta\hat{h}^{\alpha}_{\rm S}}}{Z_{N_\alpha}}\right\}P_{N_\alpha} \approx {\rm Tr}_{\rm S}\left\{\,\hat{\rm d}^{\dagger}_{\alpha i\sigma}\,\hat{\rm d}_{\alpha i'\sigma',{\rm I}}(-t'')\frac{e^{-\beta(\hat{h}^{\alpha}_{\rm S}-\mu_{\alpha,N_\alpha})}}{Z_{\mu_{\alpha,N_\alpha}}}\right\}P_{N_\alpha}. \tag{B10}$$

This approximation becomes exact in the limit of $N\to\infty$. In presence of a quasicontinuous energy spectrum of the islands, we can further drop the N_α dependence of the chemical potential, for small relative variations of N_α.

The trace in Eq. (B9) can now be evaluated in the standard way and it yields Fermi functions. Inserting the results for the traces in Eq. (B7) we obtain

$$\begin{aligned}
{\rm Tr}_{\rm S}\left\{\mathcal{P}_{N_\alpha}\dot{\hat{\rho}}^{\alpha}_{\rm red}(t)\right\} = -\frac{1}{\hbar^2}\sum_{\eta}\sum_{ki\sigma\tau}|t_{\eta\alpha\sigma}|^2|u_{\sigma\tau}(\theta)|^2\int_0^t dt''\Big\{ &e^{\frac{i}{\hbar}[-E_{\eta k}+\epsilon_{\alpha i\tau}+\alpha_{\rm g}eV_{\rm g}+U_\alpha(N_\alpha-1)]t''} \\
&\times f^{+}(\epsilon_{\alpha i\tau}-\mu_\alpha)f^{-}(E_{\eta k}-\mu_\eta)\,P_{N_\alpha}(t) + e^{-\frac{i}{\hbar}(-E_{\eta k}+\epsilon_{\alpha i\tau}+\alpha_{\rm g}eV_{\rm g}+UN_\alpha)t''} f^{-}(\epsilon_{\alpha i\tau}-\mu_\alpha)f^{+}(E_{\eta k}-\mu_\eta)\,P_{N_\alpha}(t) \\
&- e^{\frac{i}{\hbar}[-E_{\eta k}+\epsilon_{\alpha i\tau}+\alpha_{\rm g}eV_{\rm g}+U(N_\alpha-1)]t''}\;f^{-}(\epsilon_{\alpha i\tau}-\mu_\alpha)f^{+}(E_{\eta k}-\mu_\eta)\,P_{N_\alpha-1}(t) \\
&- e^{-\frac{i}{\hbar}(-E_{\eta k}+\epsilon_{\alpha i\tau}+\alpha_{\rm g}eV_{\rm g}+UN_\alpha)t''} f^{+}(\epsilon_{\alpha i\tau}-\mu_{S\alpha})f^{-}(E_{\eta k}-\mu_\eta)\,P_{N_\alpha+1}(t) + {\rm c.c.}\Big\}.
\end{aligned} \tag{B11}$$

Since we are only interested in the stationary solution of the master equation, we send $t\to\infty$ and use the Dirac identity

$$\int_0^\infty dt e^{i\omega t} = \pi\delta(\omega) + i\lim_{\eta\to 0}{\rm Im}\left(\frac{i}{\omega+i\eta}\right) \tag{B12}$$

to evaluate the integrals. Due to statistical averages, no coherences are possible in the master equation and the two complex-conjugated parts can be summed up. We find

$$\begin{aligned}\mathrm{Tr_S}\left\{\mathcal{P}_{N_\alpha}\dot{\hat{\rho}}^{\alpha}_{\infty}\right\} = 0 = -\frac{2\pi}{\hbar}\sum_{\eta}\sum_{ki\sigma\tau}|t_{\eta\alpha\sigma}|^2|u_{\sigma\tau}(\theta)|^2\{&\delta[-E_{\eta k}+\epsilon_{\alpha i\tau}+\alpha_g eV_g+U_\alpha(N_\alpha-1)]\, f^+(\epsilon_{\alpha i\tau}-\mu_\alpha)f^-(E_{\eta k}-\mu_\eta)\,P_{N_\alpha}\\ &+\delta(-E_{\eta k}+\epsilon_{\alpha i\tau}+\alpha_g eV_g+UN_\alpha)f^-(\epsilon_{\alpha i\tau}-\mu_\alpha)f^+(E_{\eta k}-\mu_\eta)\,P_{N_\alpha}-\delta[-E_{\eta k}+\epsilon_{\alpha i\tau}\\ &+\alpha_g eV_g+U(N_\alpha-1)]f^-(\epsilon_{\alpha i\tau}-\mu_\alpha)f^+(E_{\eta k}-\mu_\eta)\,P_{N_\alpha-1}-\delta(-E_{\eta k}+\epsilon_{\alpha i\tau}+\alpha_g eV_g+UN_\alpha)\\ &\times f^+(\epsilon_{\alpha i\tau}-\mu_\alpha)f^-(E_{\eta k}-\mu_\eta)\,P_{N_\alpha+1}\}.\end{aligned} \tag{B13}$$

Further, we consider the continuum limit of the states in the quantum dot

$$\sum_i \to \int_{-\infty}^{\infty} d\epsilon\, g_{\alpha\tau}(\epsilon), \tag{B14}$$

with $g_{\alpha\tau}(\epsilon)$ being the energy-dependent density of states in island α with the spin τ, defined in Eq. (6). For the leads

$$\sum_k \to \int_{-\infty}^{\infty} dE\, D_{\eta\sigma}, \tag{B15}$$

where $D_{\eta\sigma}$ is the density of states of lead η which is considered in the flat-band limit. The integration over the lead degrees of freedom gives

$$\begin{aligned}\mathrm{Tr_S}\left\{\mathcal{P}_{N_\alpha}\dot{\hat{\rho}}^{\alpha}_{\infty}\right\} = 0 = -\frac{2\pi}{\hbar}\sum_{\eta\sigma\tau}|t_{\eta\alpha\sigma}|^2|u_{\sigma\tau}(\theta)|^2 D_{\eta\sigma}\int d\epsilon\, g_{\alpha\tau}(\epsilon)\big\{&f^+\big(\epsilon-\mu_\alpha\big)f^-(\epsilon+\Delta E_{N_\alpha-1}-\mu_\eta)\,P_{N_\alpha}\\ &+f^-(\epsilon-\mu_\alpha)f^+\big(\epsilon+\Delta E_{N_\alpha}-\mu_\eta\big)\,P_{N_\alpha}-f^-(\epsilon-\mu_\alpha)f^+\big(\epsilon+\Delta E_{N_\alpha-1}-\mu_\eta\big)\,P_{N_\alpha-1}\\ &-f^+(\epsilon-\mu_\alpha)f^-\big(\epsilon+\Delta E_{N_\alpha}-\mu_\eta\big)\,P_{N_\alpha+1}\},\end{aligned} \tag{B16}$$

where $\Delta E_{N_\alpha} = UN_\alpha + \alpha_g eV_g$. In a last step we insert $g_{\alpha\tau}(\epsilon)$ [see Eq. (6) in the main text], and the remaining integral can be done by using the following identities:

$$f^+(x)f^-(y) = b^+(x-y)[f^+(y)-f^+(x)], \tag{B17}$$

$$\int_{-\infty}^{\infty} dx[f^+(x)-f^+(x+\omega)] = \omega, \tag{B18}$$

$$\begin{aligned}&\int_{-\infty}^{\infty} dx\, f^+(x+a)f^-(x+b)f^-(x+c)\\ &= \int_{-\infty}^{\infty} dx\, b^+(a-b)(f^+(x+b)-f^+(x+a))f^-(x+c)\\ &= b^+(a-b)\left\{b^+(b-c)\int_{-\infty}^{\infty} dx(f^+(x+c)-f^+(x+b))-b^+(a-c)\int_{-\infty}^{\infty} dx(f^+(x+c)-f^+(x+a))\right\}\\ &= b^+(a-b)(F(b-c)-F(a-c)).\end{aligned} \tag{B19}$$

$b^{\pm}(x)$ and $F(x)$ are defined in the main text just below Eq. (10). Using these identities yields the final result

$$\mathrm{Tr_S}\left\{\mathcal{P}_{N_\alpha}\dot{\hat{\rho}}^{\alpha}_{\infty}\right\} = 0 = \sum_{\eta\sigma}\left\{-\Gamma^{N_\alpha\to N_\alpha-1}_{\eta\alpha\sigma}P_{N_\alpha}-\Gamma^{N_\alpha\to N_\alpha+1}_{\eta\alpha\sigma}P_{N_\alpha}+\Gamma^{N_\alpha-1\to N}_{\eta\alpha\sigma}\,P_{N_\alpha-1}+\Gamma^{N_\alpha+1\to N}_{\eta\alpha\sigma}\,P_{N_\alpha+1}\right\}. \tag{B20}$$

APPENDIX C: CURRENT

Finally, we briefly outline the derivation of the current formula. The current is defined as

$$I_\eta = e\frac{d}{dt}\langle\hat{N}_\eta\rangle(t). \tag{C1}$$

In the interaction picture, the total particle-number operator of lead η, $\hat{N}_\eta$, is not evolving in time since it commutes with the unperturbed part of the Hamiltonian. Therefore, the current reads as

$$I_\eta = e\,\mathrm{Tr_{S+L}}\left\{\hat{N}_\eta\frac{d}{dt}\hat{\rho}_{\mathrm{I}}(t)\right\} = -\frac{i}{\hbar}\mathrm{Tr_{S+L}}\{\hat{N}_\eta[\hat{H}_{\mathrm{T,I}}(t),\hat{\rho}_{\mathrm{I}}(0)]\}-\frac{1}{\hbar^2}\int_0^t dt'\,\mathrm{Tr_{S+L}}\{\hat{N}_\eta[\hat{H}_{\mathrm{T,I}}(t),[\hat{H}_{\mathrm{T,I}}(t'),\hat{\rho}_{\mathrm{I}}(t')]]\}, \tag{C2}$$

where we expand $\frac{d}{dt}\hat{\rho}_{\rm I}(t)$ up to second order in $\hat{H}_{\rm T}$. The first term of Eq. (C2) vanishes since only an odd number of operators appear in the trace. In the second term, we replace $\hat{\rho}_{\rm I}(t') \to \rho_{\rm I}(t)$. Exploiting further the cyclic invariance of the trace, we find

$$I_\eta = -\frac{e}{\hbar^2}\int_0^t dt'\,\mathrm{Tr}\{[[\hat{N}_\eta, \hat{H}_{\mathrm{T,I}}(t)], \hat{H}_{\mathrm{T,I}}(t')]\hat{\rho}_{\rm I}(t)\} = -\frac{2e}{\hbar^2}\mathrm{Re}\left(\int_0^t dt'\,\mathrm{Tr}_{\mathrm{S+L}}\{[\hat{N}_\eta, \hat{H}_{\mathrm{T,I}}(t)]\hat{H}_{\mathrm{T,I}}(t')\hat{\rho}_{\rm I}(t)\}\right). \tag{C3}$$

In the last step, we exploited the anti-Hermiticity of $[\hat{N}_\eta, \hat{H}_{\mathrm{T,I}}(t)]$. Following the same steps as in the derivation of the master equation, one can identify the rates, and one finds the well-known expression of the current

$$I_\eta = -e\sum_{\alpha\sigma}\sum_{N_\alpha}\left\{\Gamma_{\eta\alpha\sigma}^{N_\alpha\to N_\alpha+1}P_{N_\alpha} - \Gamma_{\eta\alpha\sigma}^{N_\alpha\to N_\alpha-1}P_{N_\alpha}\right\}. \tag{C4}$$

APPENDIX D: CALCULATION OF THE DIFFERENTIAL CONDUCTANCE

Differentiating Eq. (15) with respect to $V_{\rm b}$ and inserting the definition of Eq. (14) yields the differential conductance of the first plateau:

$$\frac{dI_{\rm D}^{\rm P}}{d(V_{\rm b})} = \frac{2\pi e^2}{\hbar}D_0\tilde{g}_\downarrow\frac{(1-p)}{2}\frac{\alpha_{\rm D}|t_{\rm D}|^2\alpha_{\rm S}|t_{\rm S}|^2}{\alpha_D|t_{\rm D}|^2 - \alpha_{\rm S}|t_{\rm S}|^2}. \tag{D1}$$

To calculate the differential conductance at this point we differentiate Eq. (16) with respect the bias voltage and find

$$\frac{dI_D^{(\rm Q)}}{dV_{\rm b}} = -e^2\frac{\alpha\gamma + 2\beta\gamma V_{\rm b} + \beta V_{\rm b}^2}{(\gamma + \delta V_{\rm b})^2}, \tag{D2}$$

where we defined $\alpha = -\mathcal{B}_{\rm S\downarrow}\mathcal{A}_{\rm D\uparrow}$, $\beta = -\mathcal{B}_{\rm S\downarrow}(\mathcal{B}_{\rm D\uparrow} + \mathcal{B}_{\rm D\downarrow})$, $\gamma = \mathcal{A}_{\rm D\uparrow}$, and $\delta = -\mathcal{B}_{\rm S\downarrow} + \mathcal{B}_{\rm D\uparrow} + \mathcal{B}_{\rm D\downarrow}$. In order to find the value of the differential conductance plateau, we have to consider the high-bias limit and we find

$$\lim_{V_{\rm b}\to\infty}\frac{dI_S^{(\rm Q)}}{dV_{\rm b}} = -e^2\frac{\beta}{\delta} = e^2\frac{\mathcal{B}_{\rm S\downarrow}(\mathcal{B}_{\rm D\uparrow} + \mathcal{B}_{\rm D\downarrow})}{-\mathcal{B}_{\rm S\downarrow} + \mathcal{B}_{\rm D\uparrow} + \mathcal{B}_{\rm D\downarrow}}. \tag{D3}$$

Inserting back the physical constants, we find

$$\lim_{V_{\rm b}\to\infty}\frac{dI_D^{(\rm Q)}}{dV_{\rm b}} = e^2\frac{2\pi}{\hbar}D_0\tilde{g}_\downarrow\frac{(1-p)}{2}\alpha_{\rm S}|t_{\rm S}|^2\frac{\alpha_D|t_{\rm D}|^2[(1+p)\tilde{g}_\uparrow + (1-p)\tilde{g}_\downarrow]}{-(1-p)\tilde{g}_\downarrow\alpha_{\rm S}|t_{\rm S}|^2 + [(1+p)\tilde{g}_\uparrow + (1-p)\tilde{g}_\downarrow]\alpha_D|t_{\rm D}|^2}. \tag{D4}$$

[1] H. Ohno, A. Shen, F. Matsukura, A. Oiwa, A. Endo, S. Katsumoto, and Y. Iye, Appl. Phys. Lett. **69**, 363 (1996).

[2] T. Dietl and H. Ohno, Rev. Mod. Phys. **86**, 187 (2014).

[3] T. Jungwirth, J. Sinova, J. Mašek, J. Kučera, and A. H. MacDonald, Rev. Mod. Phys. **78**, 809 (2006).

[4] K. Sato, L. Bergqvist, J. Kudrnovský, P. H. Dederichs, O. Eriksson, I. Turek, B. Sanyal, G. Bouzerar, H. Katayama-Yoshida, V. A. Dinh *et al.*, Rev. Mod. Phys. **82**, 1633 (2010).

[5] C. Rüster, T. Borzenko, C. Gould, G. Schmidt, L. W. Molenkamp, X. Liu, T. J. Wojtowicz, J. K. Furdyna, Z. G. Yu, and M. E. Flatté, Phys. Rev. Lett. **91**, 216602 (2003).

[6] A. Giddings, M. Khalid, T. Jungwirth, J. Wunderlich, S. Yasin, R. Campion, K. Edmonds, J. Sinova, K. Ito, K.-Y. Wang *et al.*, Phys. Rev. Lett. **94**, 127202 (2005).

[7] M. Schlapps, M. Doeppe, K. Wagner, M. Reinwald, W. Wegscheider, and D. Weiss, Phys. Status Solidi A **203**, 3597 (2006).

[8] M. Ciorga, M. Schlapps, A. Einwanger, S. Geißler, J. Sadowski, W. Wegscheider, and D. Weiss, New J. Phys. **9**, 351 (2007).

[9] K. Pappert, S. Hümpfner, C. Gould, J. Wenisch, K. Brunner, G. Schmidt, and L. W. Molenkamp, Nat. Phys. **3**, 573 (2007).

[10] J. Wunderlich, T. Jungwirth, B. Kaestner, A. Irvine, A. Shick, N. Stone, K.-Y. Wang, U. Rana, A. Giddings, C. Foxon *et al.*, Phys. Rev. Lett. **97**, 077201 (2006).

[11] M. Schlapps, T. Lermer, S. Geissler, D. Neumaier, J. Sadowski, D. Schuh, W. Wegscheider, and D. Weiss, Phys. Rev. B **80**, 125330 (2009).

[12] D. V. Averin and K. Likharev, J. Low Temp. Phys. **62**, 345 (1986).

[13] D. V. Averin and K. K. Likharev, *Mesoscopic Phenomena in Solids* (Elsevier, Amsterdam, 1991).

[14] H. Grabert, Z. Phys. B: Condens. Matter **85**, 319 (1991).

[15] *Single Charge Tunneling*, NATO ASI Series, edited by H. Grabert and M. H. Devoret (Springer, New York, 1992).

[16] *Mesoscopic Electron Transport*, NATO ASI Series, edited by L. Sohn, L. Kouwenhoven, and G. Schön (Kluwer, Amsterdam, 1997).

[17] J. Barnaś and I. Weymann, J. Phys.: Condens. Matter **20**, 423202 (2008).

[18] K. Edmonds, P. Boguslawski, K. Wang, R. Campion, S. Novikov, N. Farley, B. Gallagher, C. Foxon, M. Sawicki, T. Dietl *et al.*, Phys. Rev. Lett. **92**, 037201 (2004).